FOURTEENTH EUROPEAN ROTORCRAFT FORUM

Paper No. 18

AN EXPERIMENTAL AND COMPUTATIONAL STUDY OF ROTOR-VORTEX INTERACTIONS

Francis X. Caradonna, Roger C. Strawn

U.S. Army Aeroflightdynamics Directorate, AVSCOM
NASA Ames Research Center
Moffett Field, California 94035 USA

John O. Bridgeman

Woodside Summit Group, Inc.
Mountain View, California, USA

20-23 September, 1988
MILANO, ITALY

ASSOCIAZIONE INDUSTRIE AEROSPAZIALI
ASSOCIAZIONE ITALIANA DI AERONAUTICA ET ASTRONAUTICA

AN EXPERIMENTAL AND COMPUTATIONAL STUDY OF ROTOR-VORTEX INTERACTIONS

Francis X. Caradonna, Roger C. Strawn

U.S. Army Aeroflightdynamics Directorate, AVSCOM
NASA Ames Research Center
Moffett Field, California 94035 USA

John O. Bridgeman

Woodside Summit Group, Inc.
Mountain View, California, USA

ABSTRACT

An experimental and computational study has been carried out where a vortex generator is located upstream of a nonlifting rotor. The vortex interacts with the rotor at at a variety of different blade azimuthal angles. Surface pressure data were measured for both oblique and parallel blade-vortex interactions (BVIs) at a number of blade tip Mach numbers and vortex miss distances. Numerical simulations were carried out for these cases with the three-dimensional, unsteady, Full-Potential Rotor code (FPR). Good agreement is seen between the experiment and computations even when the vortex strikes the rotor blade in a parallel head-on interaction. The pressure pulse at the leading edge of the rotor is shown to be the dominant feature in the BVI event for both computed and experimental results. Parallel BVIs produced in this test are shown by computation and experiment to be very similar to those produced by the rotor alone while operating in a normal descent mode.

LIST OF SYMBOLS

a = vortex core radius
AR = aspect ratio, R/c
c = rotor chord length
C = chord length for the vortex generator
C_l = lift coefficient
C_m = pitching moment coefficient
C_p = pressure coefficient
M_T = hover tip Mach number
r = spanwise distance along the rotor, also radial distance from vortex center in Eq. (1)
R = radial distance to the rotor tip
t = time
V = vortex tangential velocity
$\vec{V}_q$ = vortex velocity field in Eq. (3)
V_∞ = tunnel free stream velocity
x = chordwise distance along the rotor
X_v = distance from rotor leading edge to vortex center
X_0 = fixed vortex offset in Fig. 2
Z_v = vortex separation distance in Fig. 2
δ = vortex generator thickness
Γ = circulation for the vortex
$\hat{\Gamma}$ = vortex strength normalized by $(V_\infty C)$
μ = rotor advance ratio

Ω = rotor angular velocity

ϕ = velocity potential

ψ = rotor azimuthal angle, deg.

ρ = fluid density

1. INTRODUCTION

The flow on a helicopter rotor is complicated by the fact that it must operate in close proximity to its own wake as shown in Fig. 1. In many flight regimes this wake takes the form of a classical concentrated tip vortex. The interaction of a rotor with these tip vortices determines much of the vibratory and acoustic problems which plague helicopter operations. These blade-vortex interactions (BVIs) are characterized by high Mach numbers (greater than 0.6 and frequently transonic) and can occur for a wide variety of blade-vortex orientations. Typically, those interactions in which the blade and vortex are nearly parallel are important for acoustics, while the more oblique interactions are characteristically more gradual and can affect vibratory loading.

This paper will address the BVI problem with the aim of better understanding the physical processes involved and to investigate the various means to include BVIs in current finite-difference rotor analyses. Toward this end we shall compare surface pressure data from a special purpose rotor BVI experiment with results from a three-dimensional, unsteady full-potential rotor code (FPR). Both the experiment and the code employed were developed concurrently at the Army Aeroflightdynamics Directorate at Ames Research Center.

2. THE EXPERIMENT

Most experimental BVI investigations have involved two-dimensional setups, wherein an upstream vortex was generated either in a wind tunnel by a pitching airfoil [1,2], or in a shock tube by the starting vortex produced by the interaction of a shock with an airfoil [3,4]. The subsequent BVI on the downstream airfoil could then be observed by pressure or optical measurements. We have used an alternate approach originally employed by McCormick and Surendraiah [5] and later used by Caradonna et al. [6]. This approach employs a pressure-instrumented rotor interacting with a vortex produced by an upstream semi-span wing. A schematic of this experimental setup is shown in Fig. 2. A brief description of this test and some salient results will now follow. A more complete discussion is found in Ref. 7.

The first step in the test setup process was to locate the vortex generator so that the vortex will meet the rotor in a parallel encounter. This location serves as a reference point from which all subsequent vortex lateral offsets, X_0, are measured. The next step would normally be to measure the vortex structure and strength at appropriate locations downstream. In a previous test [6], we accomplished this using a traversing five-hole pitot probe. The present test, however, was directly preceded with a study by McAlister and Takahashi [8] of tip vortex structure using wing geometries which are very close to those of our vortex generator. We therefore always ran the vortex generator at the 12° incidence angle used by McAlister and Takahashi. This enables us to directly use their vortex measurements which encompass the effects of aspect ratio, Reynolds number, and downstream distance from the vortex generator.

Following the location and testing of the vortex generator, the rotor was then installed. Figure 3 is a photograph of the model installation in the number-2 7x10 foot wind tunnel at Ames Research Center. The vortex generator seen in the background is a telescoping semispan wing mounted on the tunnel ceiling 48 in. upstream of the rotor tip (in the $\psi = 180°$ position). The wing has an 18-in. chord and a NACA 0015 profile and is equipped with an ammonium bisulphate smoke generator to visualize the tip vortex.

The rotor model is two-bladed with a teetering hub. It is untwisted, with a diameter of 7.125 ft, a constant 6-in. chord and a NACA 0012 airfoil section. The blades were constructed almost entirely of balsa and carbon/epoxy composites to minimize aeroelastic effects. Full cyclic and collective control were provided through a swashplate controller. Remote shaft tilt capability was also incorporated in the test stand.

Figure 4 is a photograph of the tunnel and rotor in operation. The vortex generator produces a distinct, steady tip vortex, seen here highlighted by the smoke generator located in the wing tip. The wing was mounted from the tunnel ceiling to avoid having the rotor pass through the wing vorticity sheet. The rotor is operated at zero collective angle to minimize any distortion of the vortex and is trimmed

to minimum flapping. As seen in this view, the rotor hub seems to cause considerable perturbation of the vortex. However, there is no hub perturbation at the rotor tip where the main BVI occurs. This type of visualization indicates that the interaction is a simple one in which the vortex location is not greatly perturbed by the passing blade. Even head-on collisions of the vortex with the blade produce no noticeable vortex displacements during the BVI although these must certainly cause large changes in the vortex structure.

Views like those described were recorded mainly using strobe lights and video cameras. With this equipment, the vortex position and orientation relative to the blade can easily be determined. Several parameters under our control allow us to stage a variety of blade-vortex interactions. The telescoping mechanism built into the vortex generator allows the wing to be extended or retracted (during test operation) to adjust the tip-vortex height relative to the rotor. The parallel BVI shown in Fig. 4 was achieved by locating the vortex generator near the tunnel centerline such that the tip vortex produced would encounter the rotor at the $\psi = 180°$ azimuthal angle. The vortex generator can also be mounted to the left or right of the centerline to achieve oblique interactions in the second or third azimuthal quadrants.

The aerodynamic loading from the BVI was measured by subminiature pressure transducers embedded in the rotor. In all, 60 transducers were employed - 30 absolute transducers on one blade and 30 differential transducers in identical locations on the other blade. The transducers on each blade were arranged in an array of three radial stations by 10 chordwise stations. The signals from these transducers were sent (via a large slipring set) to an on-line digitizing system (a DATACOM 8234 running on a VAX 11-785) capable of acquiring 1024 words/channel/rotor revolution. Additional instrumentation provided blade root torsion and flap-bending, flap-angle, and pitch-link load data. Thirty-two revolutions of data were acquired for each test point.

Data were obtained for a range of vortex generator lateral positions and tip Mach numbers. Throughout the test the vortex generator was set to 12° incidence and nearly all cases were run at an advance ratio of 0.197. In the following discussion, we shall only discuss some typical results from the parallel and also one oblique BVI ($X_0 = 13.25$ in.) case.

Figure 5 shows the measured pressure time histories for three chordwise locations at r/R=0.893. This is a parallel BVI case in which the closest blade-vortex distance is $Z_v/c = 0.25$. On the blade upper surface (that is, on the vortex side of the blade) the pressure is measured directly by absolute pressure transducers. The lower surface pressures are obtained by subtracting the differential transducer readings from the upper surface absolute readings. On the vortex side, the BVI is most prominently seen as a sharp expansion-recompression near the leading edge at $\psi = 180°$. Elsewhere on the chord a related pressure perturbation occurs. However, these aft perturbations are far weaker and have a different shape and time scale. At the trailing edge the BVI pressure perturbation is a weak and much shorter compression-reexpansion. On the other side of the blade, the pressure history is nearly equal and opposite to that on the vortex side. On this time scale, all the BVI events seem to occur simultaneously. It is now necessary to examine the BVI on a scale of the chord transit interval.

Figure 6 shows an entire chordwise set of absolute pressure variations on the vortex side of the blade. This figure uses a much expanded azimuthal scale and also superimposes a scale showing the number of chords that the rotor travels with respect to the vortex. The origin of this auxiliary scale is set at the point of the leading edge minimum pressure. This choice of origin is based on the correlation of stroboscopic smoke visualization with the temporal pressure variations. However, it will be shown later that the association of minimum pressure with $X_v = 0$ may not be strictly correct.

The case that is shown in Fig. 6 has a tip Mach number of 0.713 and the interaction is head-on. This means that the blade slices directly through the vortex. The central event is a steep pressure rise which begins when the vortex is near the leading edge. The characteristic time for this rise is about 0.25 to 0.50 chords of travel. Downstream from the leading edge, the pressure variation diminishes drastically and alters its character. An initial pressure rise is seen in all the transducers. However, the rearmost transducers register the rise at a slightly later time. This time delay is far shorter than the vortex transit time and cannot therefore be a convective process. Therefore, we are probably seeing a downstream propagating wave which has its origin in the leading edge vortex interaction region. We have labeled this family of perturbations as a "propagated disturbance" in Fig. 6.

The tracking of pressure maxima and minima also shows the presence of two other families of events which begin to be clearly seen at transducer no. 4 (x/c=.31). One family of minima is moving downstream at a rate of 1.15 to 1.3 times the undisturbed free-stream velocity and is probably the track of the vortex (or rather half of it in this case) which is convecting at the local surface velocity. This convective family of perturbations was not seen in Ref. 6 probably because head-on encounters were

not produced then. The second family of convective disturbances seen in Fig. 6 moves at about half of free-stream velocity. This is assumed to be a local separation region induced by the passing vortex. However, we have not seen a global flow breakdown as a result of the BVI.

3. THE VORTEX STRUCTURE

An effective computer simulation of the BVI process should depend on the accuracy of the vortex model used. The previously mentioned data of McAlister and Takahashi is the basis for a computational model of the present BVI experiment. Figure 7 (derived from Ref. 8) is a plot of the tip vortex tangential velocity distributions at downstream distances of 2.0 and 4.0 chords from the trailing edge of the vortex generator. At the time of the parallel BVI the rotor tip is 3.0 chords downstream of the trailing edge. Although there is little difference between these two distributions, it is desirable to use a vortex model that fits their mean. We have chosen to use the Sculley [9] algebraic vortex model

$$V = \frac{\Gamma}{2\pi r}\left(\frac{r^2}{r^2 + a^2}\right) \tag{1}$$

where a is the maximum velocity radius, r is the radial distance from the vortex center, and Γ is the total circulation.

Srinivasan et al. [10] have previously used Eq. (1) in their BVI modeling. They have pointed out the importance of using a model which produces the correct maximum tangential velocity, V_m. Eq. (1) gives the proper V_m, equal to $0.625V_\infty$ at the measured radial distance, $r = 0.379\ \delta$, where δ is the wing thickness and $\hat{\Gamma} \equiv \Gamma/V_\infty C$, equals 0.406. This value of $\hat{\Gamma}$ is not in agreement with the measured total circulation, $\hat{\Gamma} = 0.49$ (see Ref. 7). In fact, the circulation discrepancy is clearly seen in Fig. 7 and represents an inadequacy of the above algebraic vortex model. It is seen in Fig. 7 that the assumption that all the vorticity is confined to a central core is incorrect. In fact, there exists a small radial region which contains about 20% of the total vorticity. This region shows up as a kink in the velocity distribution. However, for the present purposes of modeling the close BVI it suffices have the proper V_m. Therefore, Eq. (1) is used in all subsequent computations. The discrepancy in total circulation is not negligible however, and should be included in any total inflow computation.

Another important issue concerns the question of whether the above vortex data is truly representative of what occurs on a rotor. We can address this point by referring to the experimental study of rotor vortex structures of Tung et al. [11]. It was shown using hot-wire measurements on rotor tip vortices (about 65° old) that the characteristic core diameter (using V_m as an indicator) is about one blade thickness; and the characteristic V_m is about $0.5\Omega R$. Furthermore, the circulation distribution was typically seen to have sharp jumps from about $0.8\hat{\Gamma}$ to the final value of $\hat{\Gamma}$. These are precisely the features which McAlister has observed in his fixed wing data.

In one sense, however, the vortex generator in this experiment differs markedly from a rotor. The fixed-wing chord is three times larger than the rotor and must produce a tip vortex that is three times larger and a velocity peak which is much lower than a rotor would produce. In spite of this apparent scaling discrepancy, the artificially generated BVI seems to be quite representative of an actual rotor case. This will be discussed further in section 5.

4. THE COMPUTATIONAL METHOD

The BVI computer simulations were performed with the Full-Potential Rotor Code (FPR) developed at the U. S. Army Aeroflightdynamics Directorate. Details of the code can be found in Refs. 12 and 13. The code solves the 3-D unsteady full-potential equation for transonic flow.

$$\rho_t + \nabla \cdot (\rho \nabla \phi) = 0 \tag{2}$$

where density is determined by the unsteady Bernoulli equation.

The formulation in FPR uses a conservation form of Eq. (2) in generalized coordinates. First-order backward differencing is used for the time derivatives and second-order central differencing is used in space. A spanwise series of body-fitted parallel O-grids are used for the basic grid system. Rotor flows are computed by assigning an appropriate rotational coordinate velocity to each grid point. Upwind biasing of the density is used in regions of supersonic flow to stabilize the solution.

Typical grid sizes for the calculations in this paper are 80 points in the chordwise direction, 25 in the spanwise direction and 25 in the direction normal to the rotor surface. The finite-difference grid extends approximately four chords inward from the rotor tip and two chords outward from the tip in the spanwise direction. The outer grid boundary normal to the blade surface is located five chords from the surface of the blade. Constant time steps are used corresponding to 0.175° of rotor azimuthal angle per time step. This time step is chosen for time-accuracy considerations when the high-speed vortex is located close to the blade. The stability limit for the code is much higher, typically greater than 1.0° of azimuth per time step. In all cases, the code was initially run to find a quasi-steady starting solution about 130° azimuth ahead of the BVI location. The unsteady solution was started from this point.

The present version of the FPR code (v. 2.0) contains several improvements to the first version of the code that is described in Refs. 12 and 13. Several of these improvements are listed below.

1. Half-point differencing formulas have been implemented for both density and metric calculations. Version 1 of the code used nodal differencing for all quantities. The half-point differencing improves the accuracy and robustness of the code. This is particularly important when computing higher-order flow quantities such as drag and moment.
2. The flux-based, monotonic density biasing scheme of Shankar et al. [14] has been incorporated into the code. This new density biasing improves the stability of the code for high-speed forward flight cases.
3. Improved I/O, graphics capabilities, and documentation have been added to the code.

The vortex velocity field is specified in the FPR code using a velocity decomposition method. The total velocity field is written as the sum of a gradient of the potential, ϕ, and a known velocity field that is due to the the vortex, $\vec{V}_q$.

$$\vec{V} = \vec{V}_q + \nabla\phi \tag{3}$$

where density is still determined by the unsteady Bernoulli relation.

$$\rho = \rho(\phi_t, \vec{V}_q + \nabla\phi) \tag{4}$$

With this substitution, Eq. (2) becomes

$$\rho_t + \nabla \cdot (\rho \nabla\phi) = -\nabla \cdot \rho\vec{V}_q \tag{5}$$

Eq. (5) is then solved for the velocity potential, ϕ, which is compatible with the specified vortex velocity field, $\vec{V}_q$. The total flowfield is then determined by Eqs. (3) and (4).

This prescribed vortex velocity field comes from the model given in Eq. (1). Strictly speaking, the Bernoulli equation for density is only valid for isentropic, irrotational flow. Thus, there will be some inaccuracy in the density calculation within the rotational vortex core. This problem does not seem to be significant however, as shown by the good agreement with experimental data in the following section.

The velocity decomposition is easily implemented into the FPR code, and requires little additional computer time or memory. It has been used previously by McCroskey [15] with a 2-D small-disturbance potential code and by Srinivasan et al. [10] in a 2-D Navier-Stokes formulation. Reference 16 gives further details on the application of this velocity decomposition technique to the FPR code and demonstrates its use for 3-D BVI problems.

5. RESULTS

Previous computational BVI studies have all used two-dimensional codes (with the exception of Ref. 16, which used an earlier version of FPR) to simulate near-miss parallel BVIs. However, the present test contains a large quantity of surface pressure data which is close to the rotor tip and includes many runs with non-parallel (oblique) blade vortex orientations. Furthermore, the telescoping vortex generator permitted the running of head-on (rather than near-miss) BVIs. We shall therefore exercise these features of the data by various comparisons with FPR solutions.

The reason that previous analyses have had difficulty treating direct BVIs is twofold: 1) data were not available, and 2) few practical codes permit the computation of the inevitable vortex deformation. As previously mentioned, the FPR code shares this physical limitation. Nevertheless, FPR is sufficiently robust to compute such interactions - whether or not they are physically realistic.

Figure 8 shows the comparison of measured and computed surface pressure time histories (at $x/c = 0.02$ and 0.83, $r/R = 0.946$) for a near-miss ($Z_v/c = 0.25$) and a direct hit ($Z_v/c = 0.0$). Although there

is a difference in the steady pressure level (to be discussed shortly) the unsteady pressure components compare very closely between the data and the computations. The main difference between the data and computation is that on the upper surface (at $x/c = 0.02$) the steady pressure level is greater following the BVI. Furthermore, the data attains this final pressure level somewhat sooner than the computation. On the lower surface, for the head-on BVI, the experimental BVI induced pressure jump is steeper than computed. These differences may well be caused by vortex distortion effects. However, differences between close and head-on interactions are mainly quantitative rather than qualitative and they are well predicted by the present simple model. At x/c=0.83 the comparisons are similar. The initial BVI induced pressure jump is very well predicted by FPR. This is to be expected because this initial jump is the acoustic pulse which originates from the leading edge interaction. Following this jump, the computed and experimental pressures act differently and this certainly reflects the difference between the specified and actual vortex at this point.

The spatial pressure distributions at various points in these parallel interactions are shown in Fig. 9 ($Z_v/c = 0.25$) and Fig. 10 ($Z_v/c = 0.0$). Again, the comparison between data and computation is seen to be very good - even for the head-on BVI. The previously noted steady component pressure shift does not appear prominent on a spatial plot. The shift at the leading edge is certainly a result of the high velocity gradient there; while the trailing-edge shift seems to be a transducer offset (possibly due to an orifice burr or misalignment). The various pressure plots include the computational location of the vortex with respect to the leading edge (at $r/R = 0.946$). It is seen that the computational pressure peak (point B) coincides with the experimental peak when the vortex is somewhat upstream of the leading edge at that point. Figures 9 and 10 also show the lower-surface pressure data. We feel however that much of this lower surface data is not of quantitative significance because of orifice blockage problems in these particular transducers. The unsteady data shown in Fig. 7 are valid, however, because these particular transducers required very short orifice tubes. Subsequent comparisons will only be made with the upper surface data.

Although computing a head-on BVI may have seemed to be an extreme case for a prescribed-path vortex model (although with good results) we have also performed similar computations with vortex core sizes which are representative of real rotor vortices. Fig. 11 shows a comparison of the solutions obtained with the present experimental core size ($a/c = 0.17$) and a core which is one third of that size. The small core solution is seen to have a much greater leading edge pressure variation. Furthermore, the passing vortex becomes very conspicuous in the chordwise pressure distributions. While this demonstrates that the FPR code is robust, these kinds of pressure distributions are not typically seen in rotor BVI data.

To further investigate this issue, we have experimentally produced a self-generated BVI for a lifting rotor that matches the BVI pressure data produced by the vortex generator. This was done by scaling one of the pressure variations by the ratio of the two different vortex circulations (see Ref. 7). The resulting comparison, shown in Fig. 12, shows a similar pressure variation for the two BVI cases. Furthermore the extreme pressure variations indicative of the vortex passage (seen in Fig. 11) were not seen experimentally in self-generated BVI data. This seems to indicate that a large core size (when used with an undisturbed vortex model) is a suitable model for an actual rotor vortex interaction.

Experiment to computation comparisons have also been performed for oblique interactions. Figure 13 shows such a comparison in which the vortex generator has been offset by 0.31R to the advancing side of the rotor. The BVI encounter now occurs near $\psi = 160°$ where the Mach no. is much higher than for the parallel interactions. This is a high-speed case (hover tip Mach no. =0.763, advance ratio =0.197) in which the vortex-to-blade miss distance is $Z_v/c = 0.25$. It is seen that the leading-edge pressure jump is very well predicted as are the chordwise pressure distributions.

The previous computations have all been performed by specifying the vortex velocity field at each grid point in the computational grid. However, most rotor computations, especially with the actual rotor-generated vortex system, only specify the vortex-induced velocity field on the blade surface for simplicity. We have, therefore, repeated some of the previous computations using only a surface velocity specification of the vortex in order to test the effectiveness of this method. Figure 14 shows comparisons of computed surface pressure, lift and quarter-chord moment for a parallel (head-on) interaction. The greatest affect on pressure occurs at the leading edge where the surface specification underpredicts the pressure variation. The lift is also underpredicted by about 20%.

Figure 15 shows a similar comparison for the oblique interaction of Fig. 13. In this highly transonic case, the shock position is little affected by the vortex specification method. However, the leading edge pressure variation is now overpredicted by the surface specification method. Similar differences also occur in lift and pitching moment.

In summary, surface specifications underpredict leading edge pressure variations for a parallel BVI

and overpredicts for a transonic oblique case. In both cases, the complete vortex field specification results are in better agreement with the data. These differences would not occur with weaker interactions. However, it seems best to employ a field specification wherever possible. For the present FPR computations the field specification method has a negligible effect on storage and CPU time. For a real rotor computation, however, a more complicated vortex field would have to be recomputed for every time step which would require an increase in computer run time.

6. CONCLUSIONS

An experimental test has been conducted for the study of rotor blade-vortex interactions. The method employs a vortex generator upstream of a nonlifting rotor and permits good control and measurement of the vortex. A close matching is obtained between model and full-scale Mach and Reynolds numbers. Blade-vortex encounters have been recorded with blade pressure transducers for a range of vortex proximities, blade-vortex interaction angles and Mach numbers varying from low subsonic to transonic.

A computational model for the blade-vortex interaction has been devised. This model has been incorporated into the FPR code with either a complete field or surface velocity specification of the vortex velocities. The method is robust and provides stable solutions for extreme cases (head-on interactions with strong vorticies). The simple model for the vortex velocity field does not allow for vortex deformation during the interaction with the rotor. In spite of this, good comparisons are seen between computed solutions and experimental data. Complete field specification of the vortex velocities gives different results from the surface specified velocities when the rotor is close to the vortex. The field specification technique always gives better agreement with the experimental data.

Both experimental and computer results show that the artificially generated BVI in this test is representative of self-generated blade-vortex interactions for rotors in flight. This is true even though vortex core sizes for self-generated vorticies are smaller than the core sizes produced by the current vortex generator. This suggests that vortex distortion must have a large effect in rotor wakes. Thus, tip vorticies with increased core sizes may be good models for BVI simulations in actual rotor wakes.

The primary blade-vortex interaction event is the abrupt pressure jump near the leading edge that occurs when a rotor blade undergoes a close encounter with a well-defined vortex. This pressure pulse consists of a sudden compression on the vortex side of the blade (for the presently used vorticity sense) and a roughly equal expansion on the other side. By far, the greatest effect is at the leading edge with a rapid decrease in magnitude toward the trailing edge.

The timing of the aft transducer pressure events with respect to the leading-edge pulse gives clues concerning the various BVI processes. We have identified what is probably a downstream propagative wave and one or more convective disturbances (one of which corresponds to the vortex passage). Although these are minor compared to the leading edge event, they are useful diagnostic tools. The propagative and convective events have been identified both for externally and self-generated BVIs. This and a comparison of pulse magnitude and width demonstrates that the use of an external (and necessarily large) vortex generator accurately reproduces a rotor's self-generated parallel BVI.

7. REFERENCES

1. D. Seath, J. N. Kim and D. R. Wilson: "An Investigation of the Parallel Blade/Vortex Interaction in a Low Speed Wind Tunnel," AIAA Paper 87-1345, Honolulu, Hawaii, June 1987.
2. J. Straus, P. Renzoni, and R. E. Mayle, "Airfoil Pressure Measurements During a Blade-Vortex Interaction and a Comparison with Theory," AIAA Paper 88-0669, Reno, Nevada, Jan. 1988.
3. M. Mandella, and D. Bershader, "Quantitative Study of the Compressible Vortex: Generation, Structure and Interaction with Airfoil," AIAA Paper 87- 0328, Reno, Nevada, Jan. 1987.
4. G. E. A. Meier, and R. Timm, "Unsteady Vortex Airfoil Interaction," *Report of Max Planck Institue für Stromungsforshcung*, Göttingen, West Germany, 1986.
5. B. W. McCormick, and M. Surendraiah, "A Study of Rotor Blade-Vortex Interactions," *Presented at the 26th Annual Forum of the American Helicopter Society*, Washington, DC, June 1970.
6. F. X. Caradonna, G. H. Laub, and C. Tung, "An Experimental Investigation of the Parallel Blade-Vortex Interaction," *Presented at the 10th European Rotorcraft Forum*, The Hague, Netherlands, Aug. 1984 (See also NASA TM-86005, Nov. 1984).

7. F. X. Caradonna, J. L. Lautenschlager, and M. J. Silva, "An Experimental Study of Rotor-Vortex Interactions," AIAA Paper 88-0045, Reno, Nevada, Jan. 1988.
8. K. W. McAlister, and R. Takahashi, U. S. Army Aeroflightdynamics Directorate, Ames Research Center, Moffett Field, CA, (personal communication).
9. M. P. Sculley, "Computation of Helicopter Rotor Wake Geometry and Its Influence on Rotor Harmonic Loads," ASRL TR-178-1, Massachusetts Institute of Technology, Mar. 1975.
10. G. R. Srinivasan, W. J. McCroskey, and J. D. Baeder, "Aerodynamics of Two-Dimensional Blade-Vortex Interaction," *AIAA Journal*, Vol. 24, No. 10, Oct. 1986, pp. 1569-1576.
11. C. Tung, S. L. Pucci, F. X. Caradonna, and H. A. Morse, "The Structure of Trailing Vortices Generated by Model Rotor Blades," *Vertica* Vol. 7, No. 1, 1983, pp. 33-43.
12. R. C. Strawn, and F. X. Caradonna,"A Conservative Full-Potential Model for Unsteady Transonic Rotor Flows," *AIAA Journal* Vol. 25, No. 2, Feb. 1987, pp. 193-198.
13. R. C. Strawn and C. Tung, "Prediction of Unsteady Transonic Rotor Loads with a Full-Potential Rotor Code," *Presented at the 43rd Annual Forum of the American Helicopter Society*, May 18-20, 1987, St. Louis, MO.
14. V. Shankar, H. Ide, J. Gorski, and S. Osher, "A Fast, Time-Accurate, Unsteady Full Potential Scheme," *AIAA Journal* Vol. 25, No. 2, Feb. 1987, pp. 230-238.
15. W. J. McCroskey, "The Effects of Gusts on the Fluctuating Airloads of Airfoils in Transonic Flow," AIAA Paper 84-1580, Snowmass, CO, June, 1984.
16. R. C. Strawn, and C. Tung, "The Prediction of Transonic Loading on Advancing Helicopter Rotors," *Presented at the AGARD/FDP Symposium on Applications of Computational Fluid Dynamics in Aeronautics*, Aix-en-Provence, France, April 1986 (See also NASA TM-88238, April 1986).

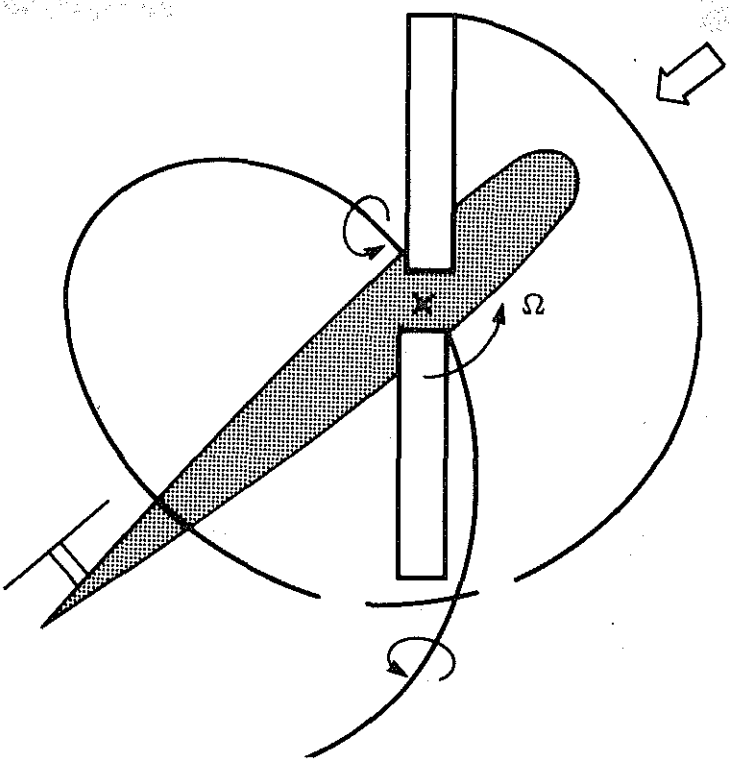

Fig. 1 The rotor blade-vortex interaction in forward flight.

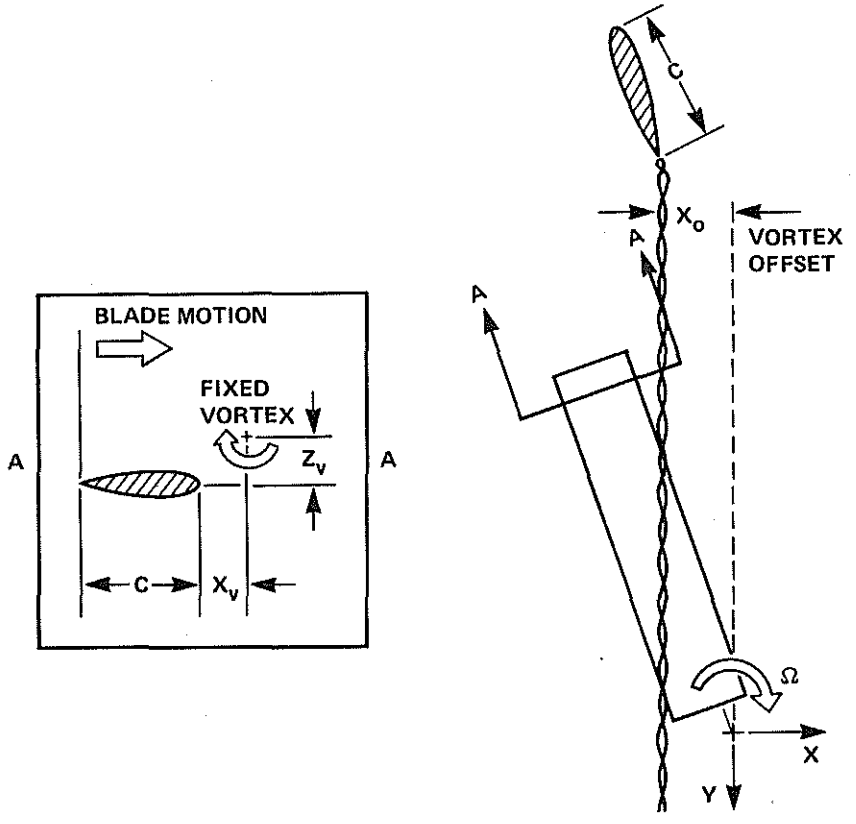

Fig. 2 A schematic of the rotor BVI test.

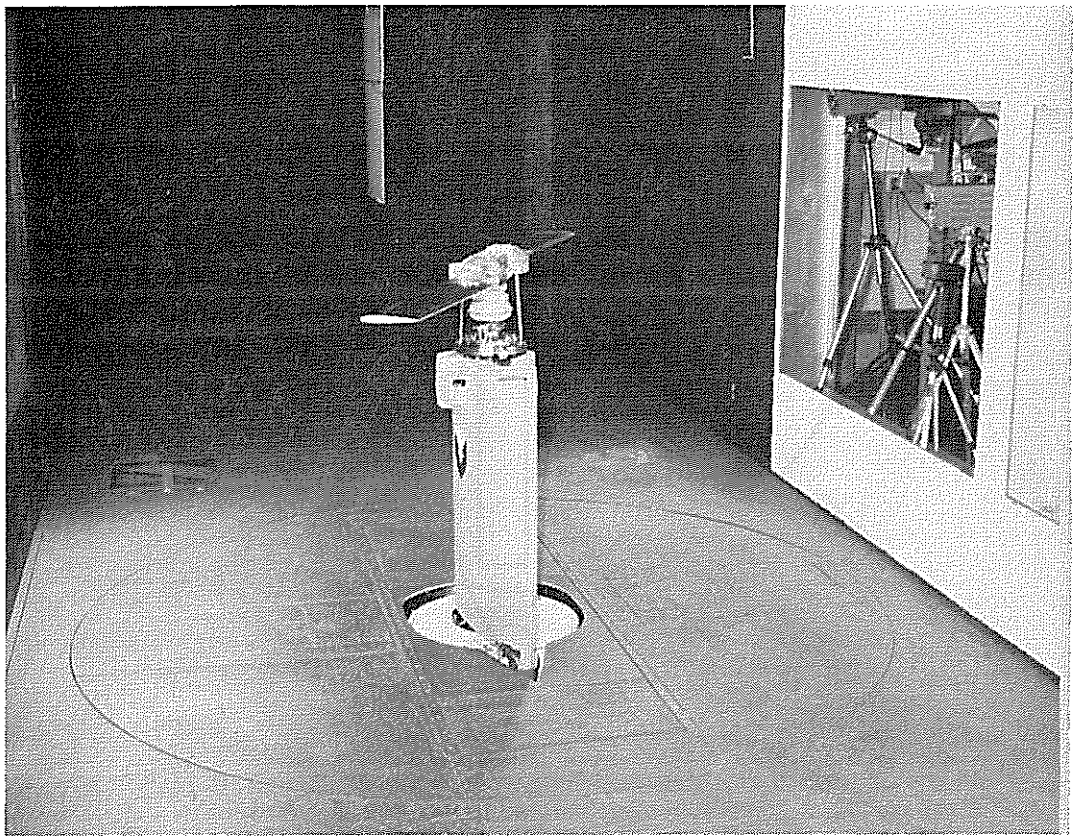

Fig. 3 The set-up of the BVI test in the Ames Research Center No. 2 7-by-10 Foot Wind Tunnel.

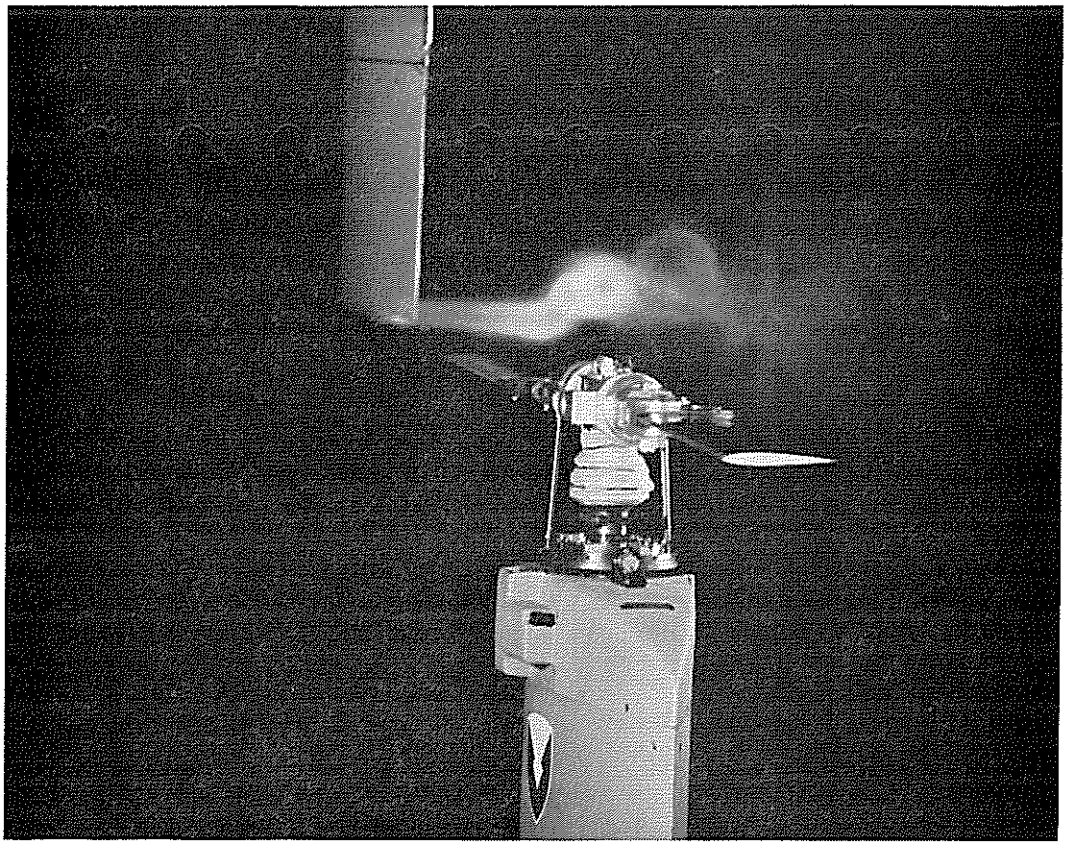

Fig. 4 The rotor and vortex generator in operation for a parallel interaction.

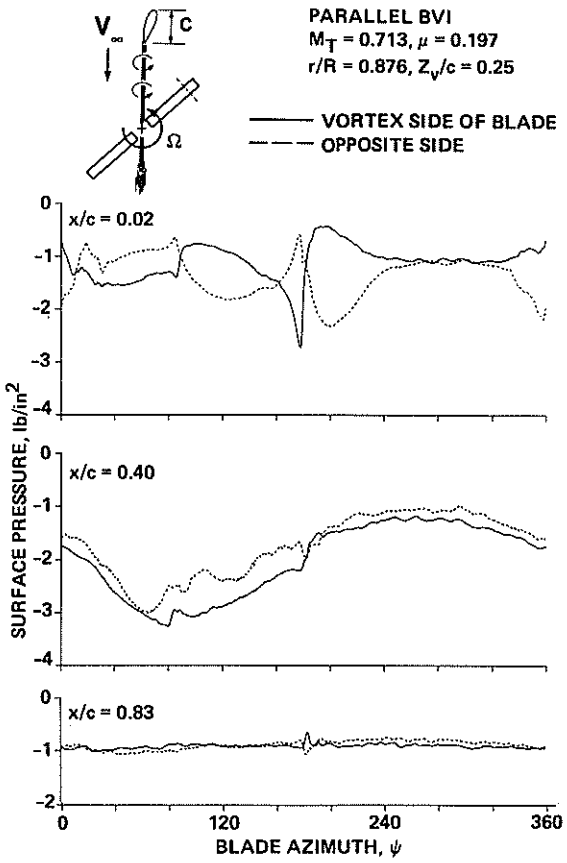

Fig. 5 Pressure variations on a rotor resulting from a parallel BVI, $M_T = 0.713$, $\mu = 0.197$, $AR = 7.125$, $r/R = 0.876$, $Z_v/c = 0.25$.

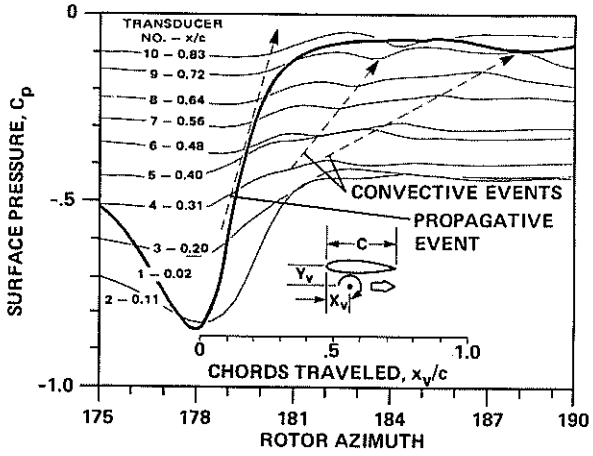

Fig. 6 Pressure variations on a rotor resulting from a parallel BVI, $M_T = 0.713$, $\mu = 0.197$, $AR = 7.125$, $r/R = 0.946$, $Z_v/c = 0.0$.

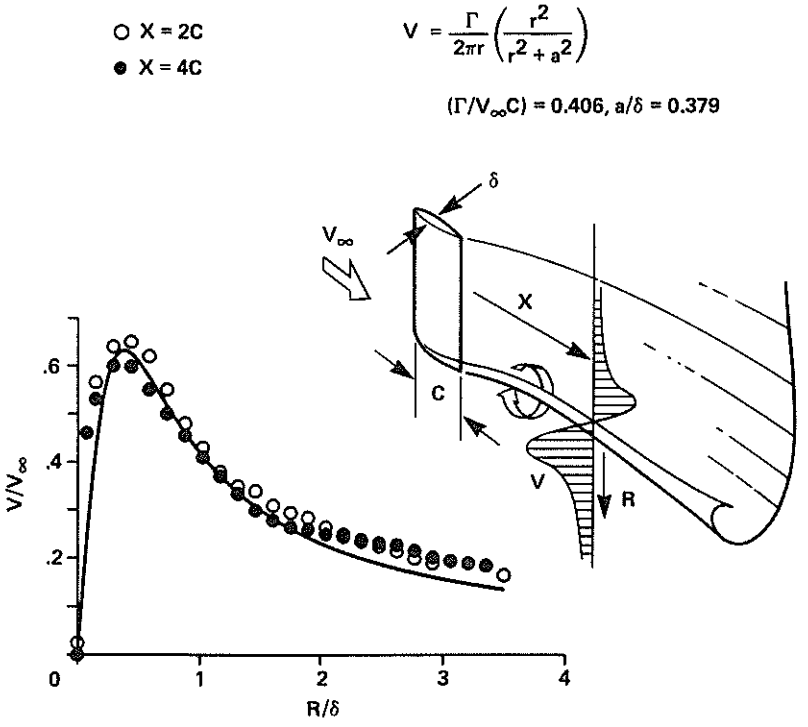

Fig. 7 Measured tangential velocities in the upstream-generated tip vortex. $\Gamma/V_\infty C = 0.406$, $a/\delta = 0.379$.

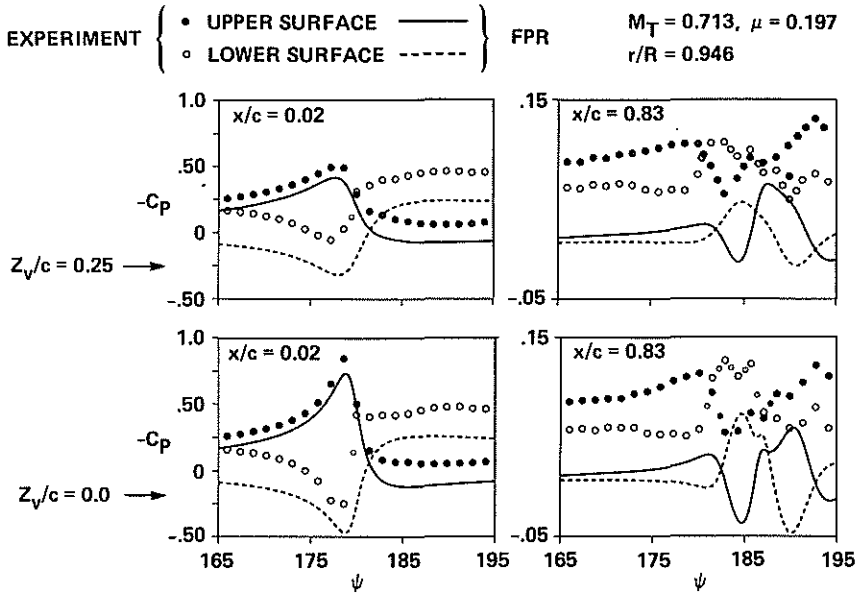

Fig. 8 Computation and experimental comparison for a parallel rotor BVI, $M_T = 0.713$, $\mu = 0.197$, $AR = 7.125$, $r/R = 0.946$.

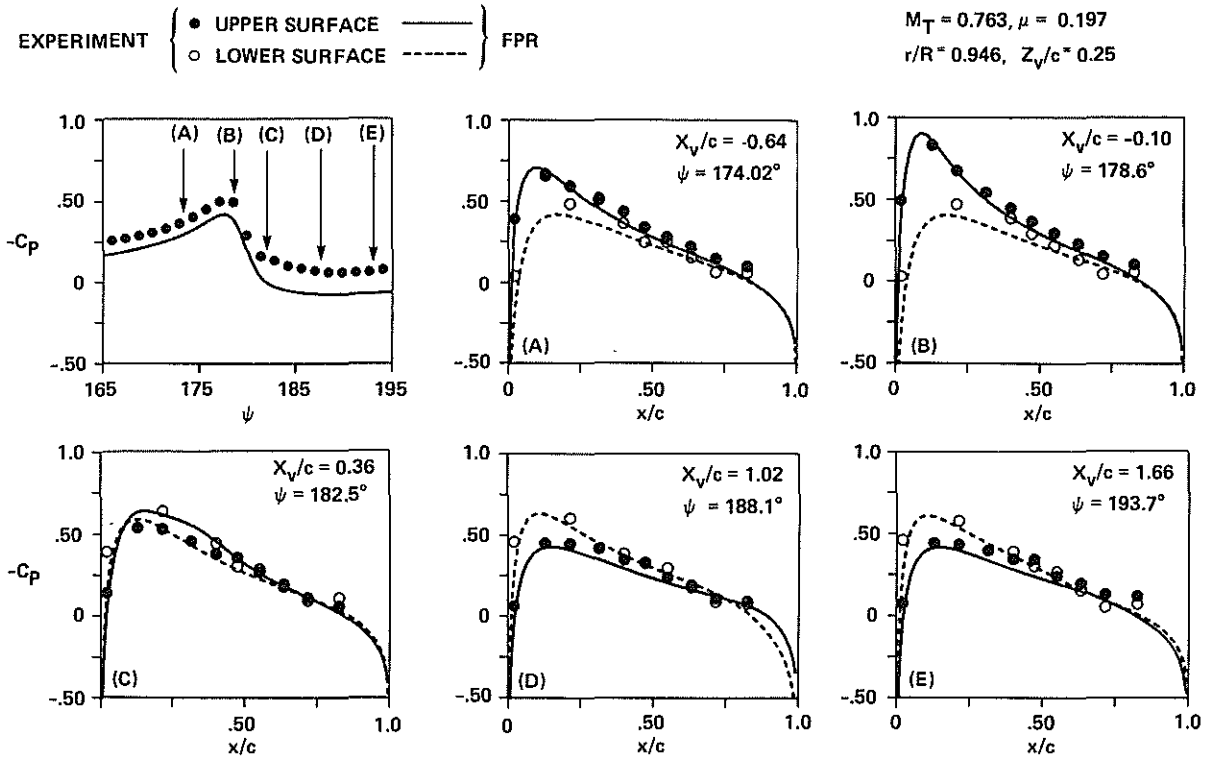

Fig. 9 Computation and experimental comparison for a parallel rotor BVI, $M_T = 0.713$, $\mu = 0.197$, $AR = 7.125$, $r/R = 0.946$, $Z_v/c = 0.25$.

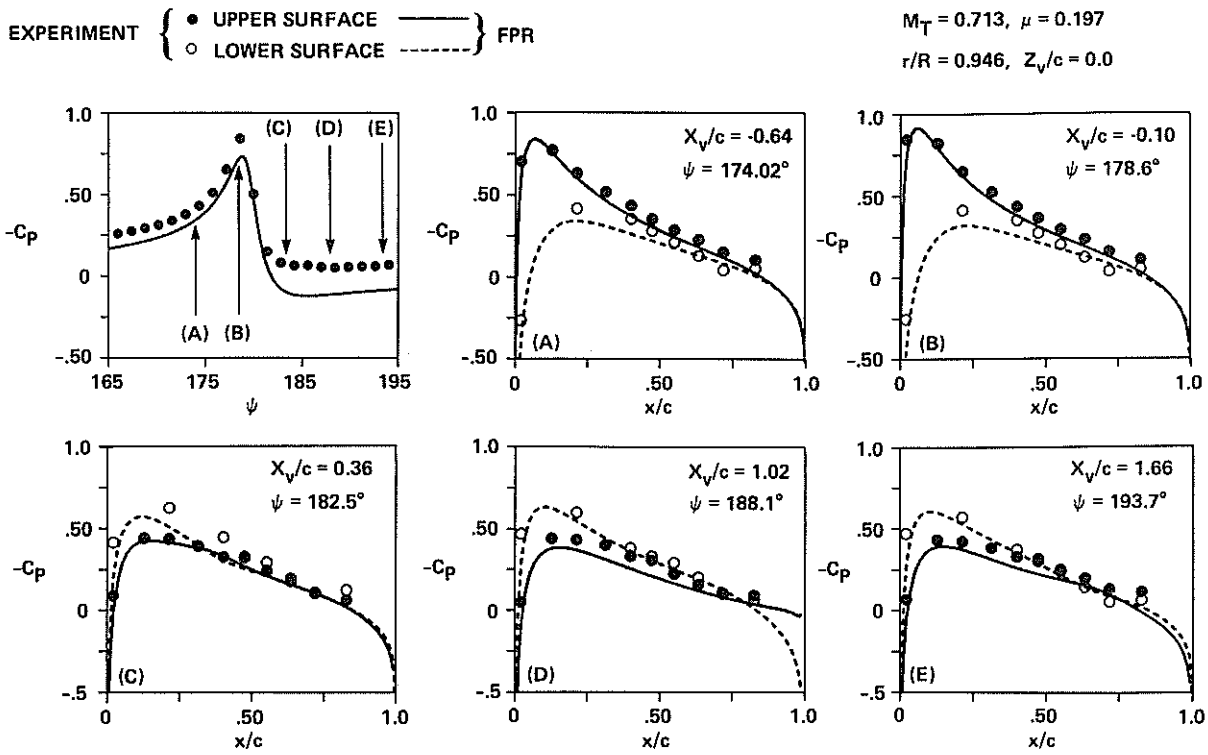

Fig. 10 Computation and experimental comparison for a parallel rotor BVI, $M_T = 0.713$, $\mu = 0.197$, $AR = 7.125$, $r/R = 0.946$, $Z_v/c = 0.0$.

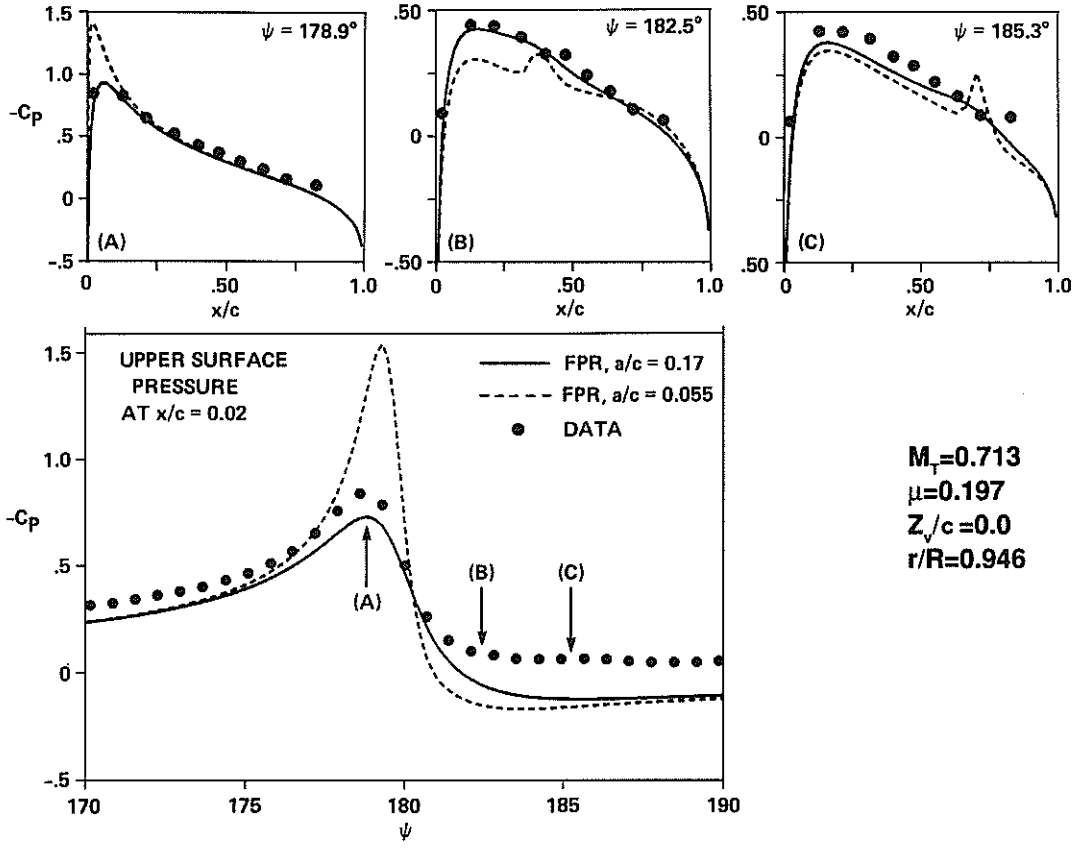

Fig. 11 Comparison of vortex core sizes for a computed parallel BVI, $M_T = 0.713$, $\mu = 0.197$, $AR = 7.125$, $r/R = 0.946$, $Z_v/c = 0.25$.

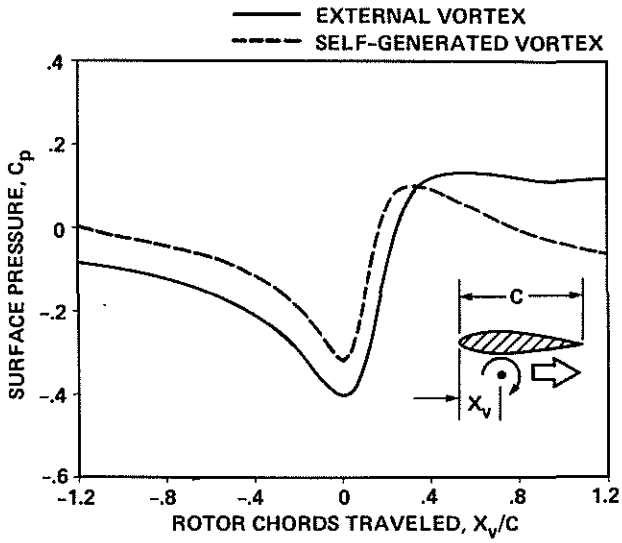

Fig. 12 A comparison of parallel BVIs with external and self-generated vorticies.

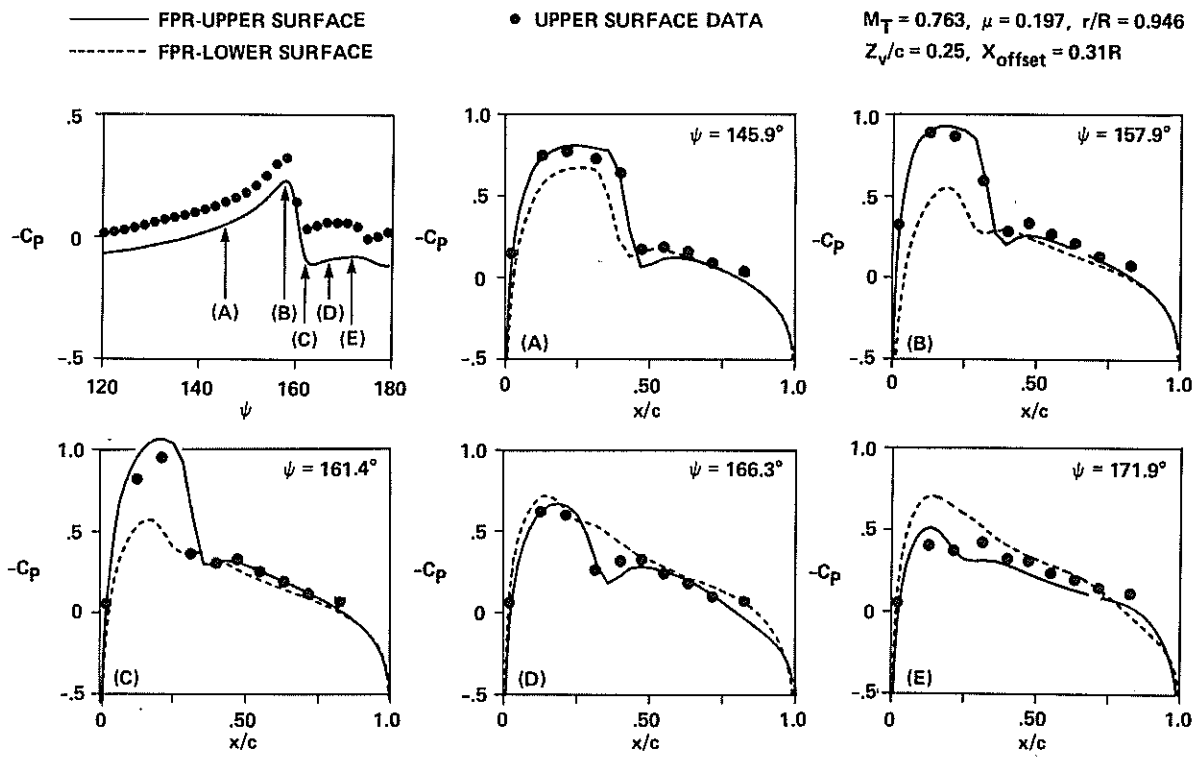

Fig. 13 Computation and experimental comparison for an oblique rotor BVI, $M_T = 0.763$, $\mu = 0.197$, $AR = 7.125$, $r/R = 0.946$, $Z_v/c = 0.25$, $X_0/c = 2.13$.

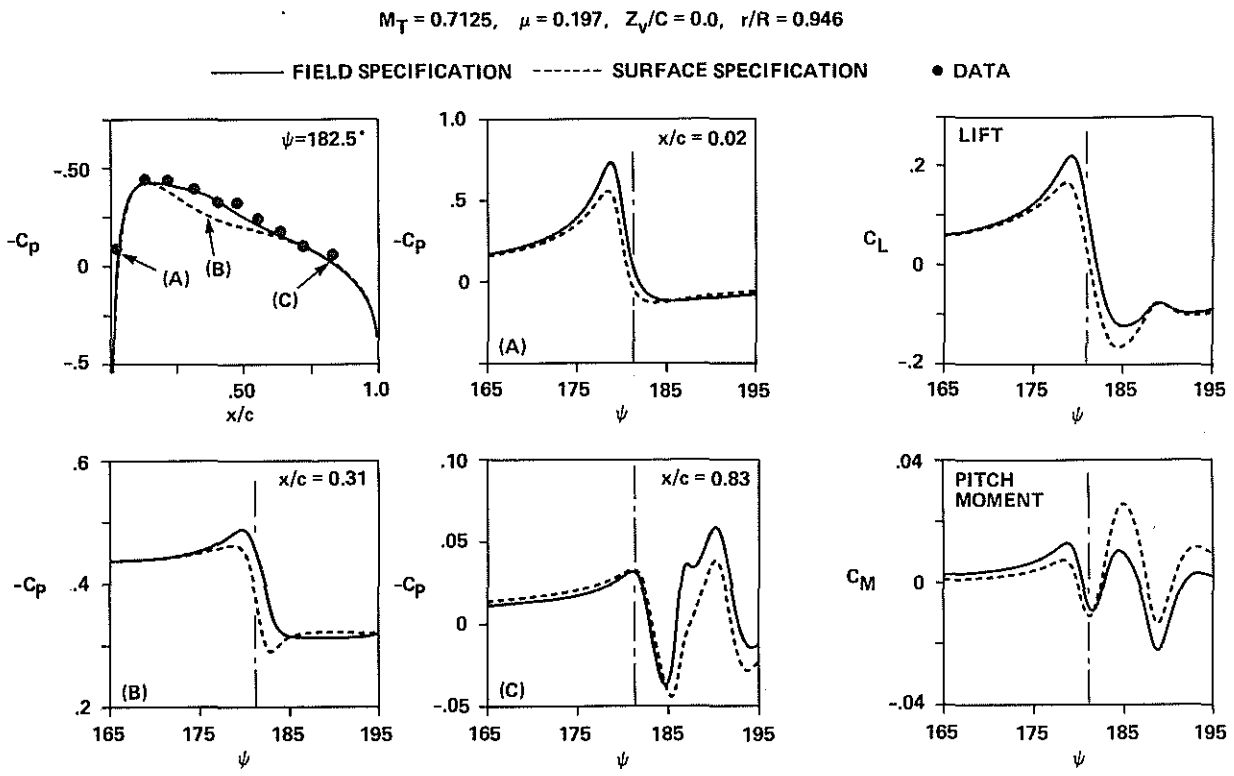

Fig. 14 The effect of vortex specification method on pressures and loads for a parallel BVI, $M_T = 0.713$, $\mu = 0.197$, $AR = 7.125$, $r/R = 0.946$, $Z_v/c = 0.0$.

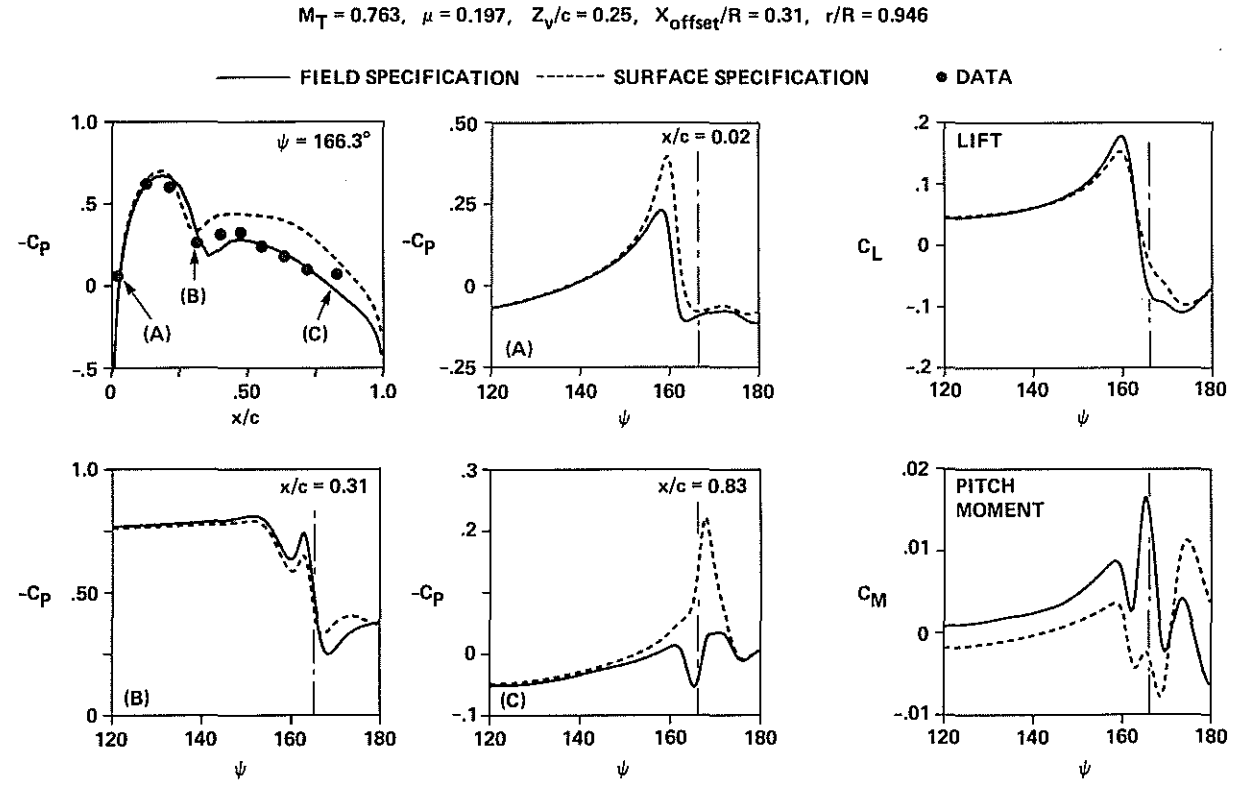

Fig. 15 The effect of vortex specification method on pressures and loads for an oblique BVI, $M_T = 0.763$, $\mu = 0.197$, $AR = 7.125$, $r/R = 0.946$, $Z_v/c = 0.25$, $X_0/c = 2.13$.